

Unifying Appearance Codes and Bilateral Grids for Driving Scene Gaussian Splatting

Nan Wang^{*,6,11}, Yuantao Chen^{8,11}, Lixing Xiao¹⁰, Weiqing Xiao^{2,11}, Bohan Li^{4,5},
Zhaoxi Chen³, Chongjie Ye⁸, Shaocong Xu¹, Saining Zhang^{1,3}, Ziyang Yan⁹
Pierre Merriaux¹², Lei Lei¹², Tianfan Xue⁷, Hao Zhao^{†,1,11}
bigcileng@gmail.com^{*}, zhaohao@air.tsinghua.edu.cn[†]

¹AIR, Tsinghua University; ²Beihang University; ³Nanyang Technological University
⁴Shanghai Jiao Tong University; ⁵Eastern Institute of Technology, Ningbo ⁶Tongji University
⁷The Chinese University of Hong Kong; ⁸The Chinese University of Hong Kong, Shenzhen
⁹University of Trento; ¹⁰Zhejiang University; ¹¹Lightwheel AI; ¹²LeddarTech

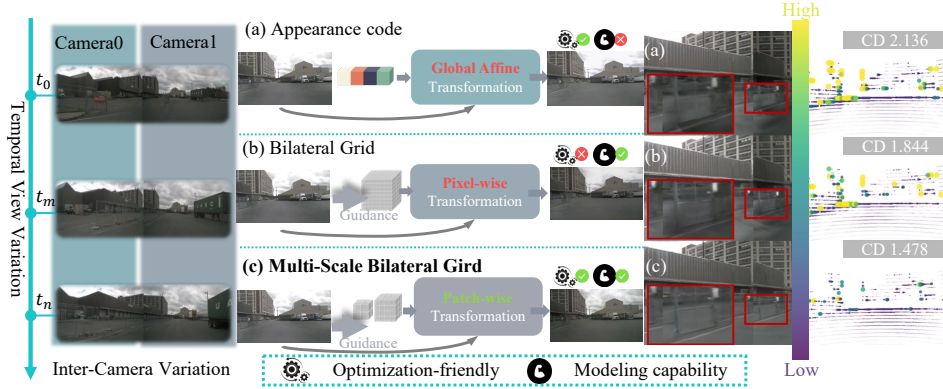


Figure 1: (a) Appearance codes rely on global affine transformations but have limited modeling capability. (b) Bilateral grids perform pixel-wise transformations, improving photometric consistency but are challenging to optimize. (c) The proposed multi-scale bilateral grid unifies appearance codes and bilateral grids, enabling patch-wise transformations.

Abstract

Neural rendering techniques, including NeRF and Gaussian Splatting (GS), rely on photometric consistency to produce high-quality reconstructions. However, in real-world scenarios, it is challenging to guarantee perfect photometric consistency in acquired images. Appearance codes have been widely used to address this issue, but their modeling capability is limited, as a single code is applied to the entire image. Recently, the bilateral grid was introduced to perform pixel-wise color mapping, but it is difficult to optimize and constrain effectively. In this paper, we propose a novel multi-scale bilateral grid that unifies appearance codes and bilateral grids. We demonstrate that this approach significantly improves geometric accuracy in dynamic, decoupled autonomous driving scene reconstruction, outperforming both appearance codes and bilateral grids. This is crucial for autonomous driving, where accurate geometry is important for obstacle avoidance and control. Our method shows strong results across four datasets: Waymo, NuScenes, Argoverse, and PandaSet. We further demonstrate that the improvement in geometry is driven by the multi-scale bilateral grid, which effectively reduces floaters caused by photometric inconsistency. Our code is open-sourced at <https://bigcileng.github.io/bilateral-driving>.

[†]Corresponding author.

1 Introduction

Neural rendering techniques, such as NeRFs [22, 34, 44, 18, 45] and Gaussian Splatting (GS) [12, 2, 6, 47, 26], have demonstrated significant potential in producing high-quality 3D reconstructions by leveraging photometric consistency. However, ensuring photometric consistency across images in real-world scenarios remains a challenge, as lighting conditions, viewpoints, and camera settings can vary considerably [21, 46, 13, 33]. In autonomous driving applications [42, 38, 32, 5, 15, 11, 31], these challenges are amplified due to the presence of multiple cameras capturing the same scene from different angles over time. As illustrated in the left half of Teaser. 1, we observe that these variations—whether temporal (across different time steps) or inter-camera (across different viewpoints)—can introduce significant discrepancies in image appearance. These inconsistencies pose difficulties in accurately reconstructing dynamic driving environments.

To address this issue, appearance codes [32, 21, 5] have been introduced to encode per-image information and assist in correcting the photometric discrepancies. These codes, while effective, have limitations in modeling capability since they apply a single transformation across the entire image, often neglecting local variations that may occur in complex scenes. For example, in dynamic scenes, such as those encountered in autonomous driving environments, lighting and viewpoints can change across different camera angles and time frames. As shown in the right top of Teaser. 1, a global affine transformation based on a single appearance code may not be sufficient to handle such variations (In Teaser. 1 NuScenes (a), the fence is blurred).

Recent advancements [35, 8] have introduced bilateral grids to perform pixel-wise transformations, enabling improved photometric consistency by allowing more localized adjustments. However, these grids face significant challenges in optimization, as they require complex constraints to avoid instability during training (As shown in Teaser. 1 (b), bilateral grids fail to effectively optimize the reconstruction of large, complex scenes.). In this work, we propose a novel solution—a multi-scale bilateral grid—integrating the strengths of appearance codes and bilateral grids. As shown in Teaser. 1, this new approach allows for patch-wise transformations. Interestingly, in extreme cases, the multi-scale bilateral grid naturally converges to either the bilateral grid or appearance code, depending on the scale. At the finest scale, the multi-scale grid behaves like a traditional bilateral grid, performing pixel-wise transformations to adjust for local variations. In contrast, at the coarsest scale, it effectively reverts to a more global transformation, resembling the behavior of appearance codes. This flexible, scale-dependent approach offers the best of both worlds, providing localized fine-tuning where necessary, while maintaining global consistency when appropriate.

We demonstrate that the multi-scale bilateral grid significantly enhances the geometric accuracy of dynamic, decoupled driving scenes, which is essential for autonomous driving applications where precise geometry plays a crucial role in tasks like obstacle avoidance and path planning. This is evidenced by our evaluation on multiple widely used datasets, including Waymo [27], NuScenes [1], Argoverse [37], and PandaSet [39]. The corresponding Chamfer Distance (CD) values, displayed in the Teaser. 1, highlight a marked reduction in error and improvement in reconstruction quality. Additionally, our method reduces photometric inconsistency, mitigating the appearance of floaters and enhancing the overall realism of the scene.

The contributions of this paper are as follows: **First**, we introduce a novel multi-scale bilateral grid that unifies appearance codes and bilateral grids, transitioning to either of the two paradigms in extreme cases, thus enhancing both modeling capability and optimization efficiency. **Second**, we show that by addressing photometric inconsistencies, it improves the geometric accuracy of dynamic, decoupled driving scene reconstructions. **Third**, we provide extensive benchmarking across four widely used datasets—Waymo, NuScenes, Argoverse, and PandaSet—where our method outperforms previous approaches, showcasing notable improvements in both qualitative and quantitative results.

2 Related Works

2.1 Bilateral Grids and Appearance Codes

Recent advancements in bilateral grids and appearance codes have significantly influenced techniques for addressing photometric inconsistencies, which are particularly critical in dynamic environments such as autonomous driving. The bilateral grids, first introduced for real-time edge-aware image processing [4], enable efficient manipulation of spatial and intensity variations, forming the foundation

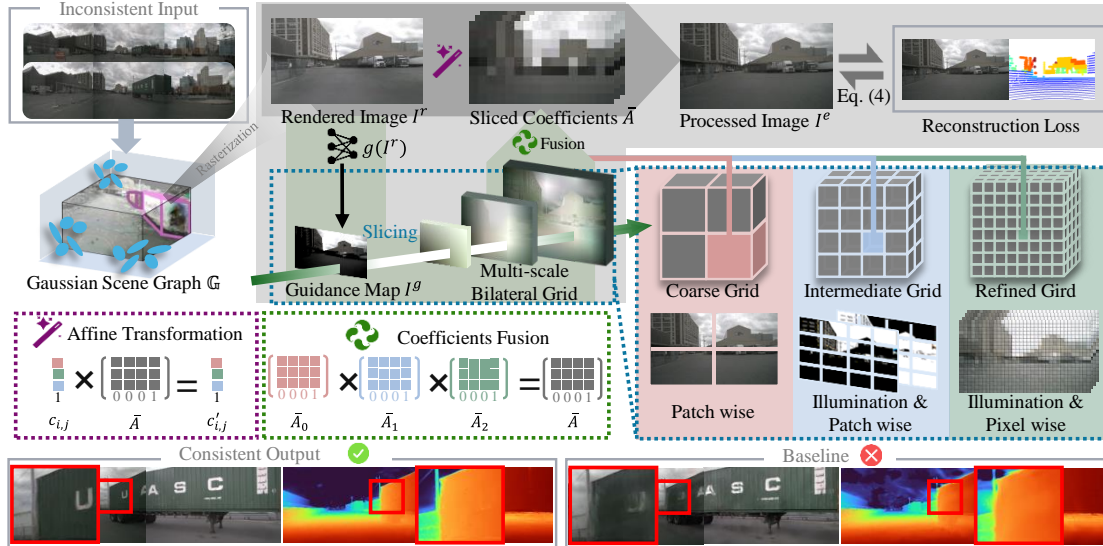


Figure 2: **Overview of our method.** We unify appearance codes with multi-scale bilateral grids. Initially, a coarse rendering is obtained from a Gaussian scene graph. This rendered image is then processed by our multi-scale bilateral grids to perform detailed per-pixel color modeling, guided by a luminance-based map through slice and fusion operations.

for many modern techniques [8, 20, 3, 40, 48]. Extensions like deep bilateral learning [8] further enhance this framework by predicting local affine transformations in bilateral space, achieving real-time image enhancement on resource-constrained devices. Similarly, bilateral-guided upsampling [3] and cost volume refinement [40] have proven effective in tasks ranging from high-dynamic-range imaging to stereo matching, demonstrating the versatility of bilateral representations. In the context of neural rendering, methods such as NeRF [28, 10, 21] and Gaussian Splatting (GS) [46, 13] have achieved groundbreaking results in novel view synthesis but photometric inconsistency caused by varying illumination or transient occluders [21, 46] remains a challenge. Techniques like bilateral guided radiance field processing [35] address these issues by disentangling camera-specific enhancements and reapplying them consistently in 3D space. WildGaussians [13] integrates DINO-based appearance codes into 3D GS to robustly handle occlusions and dynamic lighting in uncontrolled scenes. Cross-Ray NeRF [43] employs cross-ray feature covariance and grid-based transient masking to harmonize appearance variations and suppress occlusions in unconstrained image collections. Despite these strides, existing approaches often struggle to balance global consistency with localized adaptability. For instance, while appearance codes provide global adjustments, they lack the granularity to model fine-grained variations [7]. Conversely, bilateral grids excel at pixel-wise transformations but are challenging to optimize effectively [25]. To address this issue, we introduce a multi-scale bilateral grid which unifies bilateral grids and appearance codes, facilitating high-quality dynamic autonomous driving scene reconstruction with enhanced modeling capability and optimization efficiency.

2.2 Autonomous Driving Simulation

Autonomous driving simulation has emerged as a critical tool for developing perception, planning, and control systems by generating diverse, realistic driving scenarios [38, 24, 41, 17, 30, 15]. Recent advancements focus on photorealistic rendering, dynamic scene modeling, and multi-modal sensor simulation [38, 14, 50, 32, 41]. For instance, MARS [38] employs a modular NeRF-based framework to independently control static and dynamic scene elements, while Street Gaussian [41] achieves real-time urban scene rendering using explicit 3D Gaussian representations. DrivingGaussian [50] enhances dynamic scene reconstruction via composite Gaussian Splatting, ensuring occlusion accuracy and multi-camera consistency. NeuRAD [32] integrates sensor-specific effects (*e.g.*, rolling shutter, LiDAR beam divergence) to improve novel view synthesis. Holistic scene understanding and editing have also seen progress. HUGS [49] combines static and dynamic 3D Gaussians for real-time semantic parsing. ChatSim [36] enables language-driven scene editing with external asset integration.

LiDAR data integration has advanced through methods like LiDAR-NeRF [29], which uses structural regularization for low-texture regions. HO-Gaussian [16], which merges grid-based volumes with Gaussian Splatting to eliminate Structure-from-Motion (SfM) dependencies.

Despite progress, gaps persist between simulated and real-world data [17, 30]. AlignMiF [30] addresses LiDAR-camera misalignments via geometry-aligned implicit fields, while RodUS [23] decomposes urban scenes into static and dynamic components using 4D semantics to reduce artifacts. Innovations in large-scale generation include InfiniCube [19], which leverages sparse-voxel representations for unbounded dynamic scenes, and Omnire [5], which reconstructs diverse dynamic objects (*e.g.*, pedestrians) for human-vehicle interaction simulations. Furthermore, recent works like GaussianPro [6] and SplatAD [9] explore to refine 3D GS for real-time rendering of dynamic scenes. GaussianPro [6] introduces progressive propagation for texture-less surfaces, and SplatAD [9] models sensor-specific phenomena (*e.g.*, rolling shutter, LiDAR intensity). In this work, we aim to reconstruct high-quality driving scenes by unifying appearance codes and bilateral grids to enhance photometric consistency and modeling capability.

3 Methodology

3.1 Problem Formulation

We aim to reconstruct a 3D scene representation \mathbb{G} from multi-view images and LiDAR depth maps, commonly available in autonomous driving datasets. Given a set of images $\{I_{c,t}\}$ and corresponding depths $\{D_{c,t}\}$ captured by N cameras over T time steps, we formulate our objective as minimizing the discrepancy between rendered and observed images and depths:

$$\min_{\mathbb{G}} \sum_{c,t} (\|I_{c,t}^r - I_{c,t}\|_2^2 + \lambda_D \|D_{c,t}^r - D_{c,t}\|_2^2) , \quad (1)$$

where $I_{c,t}^r$ and $D_{c,t}^r$ are the rendered appearance and geometry of the scene \mathbb{G} from camera c at time t , and λ_D is a weight balancing the depth term.

However, dynamic driving scenes and varying camera properties cause inconsistent appearances, leading to geometric and texture artifacts. To address inconsistency, we decompose each image $I_{c,t}$ into consistent $\mathcal{C}_{c,t}$ (*e.g.*, intrinsic scene colors and constant sensor adjustments like normalization exposure), and non-consistent $\mathcal{N}_{c,t}$ (*e.g.*, components-varying lighting conditions, different camera settings and diverse image ISP effects):

$$I_{c,t} = \mathcal{C}_{c,t} + \mathcal{N}_{c,t} , \quad (2)$$

We model $\mathcal{N}_{c,t}$ as a non-linear transformation $\mathcal{F}(\mathcal{C}_{c,t})$. Substituting into Eq. (2):

$$I_{c,t} = \mathcal{C}_{c,t} + \mathcal{F}(\mathcal{C}_{c,t}) , \quad (3)$$

Let $\mathcal{E}(\mathcal{C}_{c,t}) = \mathcal{C}_{c,t} + \mathcal{F}(\mathcal{C}_{c,t})$, we can reformulate the optimization objective in Eq. (1) as:

$$\min_{\mathbb{G}} \sum_{c,t} (\|\mathcal{E}(\mathcal{C}_{c,t}) - I_{c,t}\|_2^2 + \lambda_D \|D_{c,t}^r - D_{c,t}\|_2^2) , \quad (4)$$

This reformulation links photometric and geometric consistency optimization within a joint objective, guiding $\mathcal{C}_{c,t}^r$ adjustments by geometric constraints ($D_{c,t}^r$). This mitigates texture-geometry ambiguities (*e.g.*, shadows on road surfaces misinterpretable as geometry changes). $\mathcal{F}(\mathcal{C}_{c,t})$ models transient appearance, while $\mathcal{C}_{c,t}^r$ enforces consistent scene properties. Experiments (Sec. 4, Tab. 1) show this joint optimization reduces both photometric error and geometric drift in comparison to baselines.

3.2 Gaussian Splatting for Autonomous Driving Environments

Following prior methodologies [5, 32], we represent autonomous driving environments using a hybrid scene graph, decomposing the scene into sky, background, and dynamic object models. Each dynamic object is represented by a 3D model in canonical space and transformed to the scene with an associated sequence of SE(3) transformations. We derive the transformation matrixes from existing object detection pipelines or ground-truth annotations.

For the sky, we use an environment map to model sky color based on viewing direction, while static background is represented as a set of semi-transparent 3D Gaussians. Each Gaussian is characterized

by a learnable opacity parameter $o \in (0, 1)$, a mean position $\mu \in \mathbb{R}^3$, and an anisotropic covariance matrix $\Sigma \in \mathbb{R}^{3 \times 3}$ which is parameterized by a scale vector $S \in \mathbb{R}^3$ and a rotation quaternion $q \in \mathbb{R}^4$. Additionally, Spherical harmonics coefficients $c \in \mathbb{R}^F$ are used to model appearance.

For the moving object models, we further distinguish between non-deformable (*e.g.*, vehicles) and deformable objects (*e.g.*, pedestrians). Non-deformable objects $\{\mathbb{G}_i^N | i \in \{1, \dots, n_n\}\}$ are optimized in their local coordinate space and transformed into the global world space via their pose T :

$$\mathbb{G}_i^N = T \otimes \hat{\mathbb{G}}_i^N, \quad (5)$$

For deformable objects $\{\mathbb{G}_i^D | i \in \{1, \dots, n_d\}\}$, we employ a deformation network \mathcal{F}_Φ (parameterized by Φ) to adapt the Gaussian representation based on latent variable e and time t :

$$\mathbb{G}_i^D = T \otimes \left(\hat{\mathbb{G}}_i^D \oplus \mathcal{F}_\Phi(\hat{\mathbb{G}}_i^D, e, t) \right). \quad (6)$$

3.3 Multi-Scale Bilateral Grid for Appearance Enhancement

Solving the photometric correction problem formulated in Eq. (4) fundamentally depends on the ability to effectively model the complex and spatially-varying photometric transformations present in real-world driving scenes. The function $\mathcal{E}(\cdot)$ in our formulation represents this crucial photometric enhancement process. To address this, we propose the Multi-Scale Bilateral Grid architecture, detailed in this section, as a novel grounded solution for approximating $\mathcal{E}(\cdot)$ and achieving high-quality, consistent appearance enhancement.

3.3.1 Multi-Scale Bilateral Grid Architecture

To address limitations of existing methods in handling diverse photometric variations in driving scenes, we propose a multi-scale bilateral grid framework. Our framework achieves this unification by employing a hierarchical pyramid of bilateral grids, organized across multiple scales. This multi-scale design is directly inspired by the nature of photometric inconsistencies in real-world environments, which range from global scene-level changes to highly localized variations (*e.g.*, from overall lighting shifts to fine texture-level shadows). By utilizing this grid hierarchy, our framework aims to capture and effectively correct photometric variations at their corresponding scales, thus enabling a more comprehensive and spatially adaptable photometric correction.

The multi-scale bilateral grid transformation can be formulated as $I^e = \bar{A} \odot I^r$, where \bar{A} represents a composite, scale-dependent photometric transformation. Crucially, this composite transformation is constructed hierarchically, combining transformations learned by individual bilateral grids at different scales, progressing from coarse to fine. This staged composition is key to achieving scale-dependent adaptation to photometric inconsistencies and allows us to move beyond the inherent limitations of single-scale methods. Further details are provided in the subsequent sections.

Our framework achieves this hierarchical representation using a three-level bilateral grid pyramid (Fig. 2): **(1) Coarse Level** ($2 \times 2 \times 1 \times 12$ grid) captures global scene structure and approximate global appearance codes; **(2) Intermediate Level** ($4 \times 4 \times 2 \times 12$ grid) represents regional features and capture mid-range photometric variations; **(3) Fine Level** ($8 \times 8 \times 4 \times 12$ grid) encodes local details and approximate pixel-wise bilateral grids within the multi-scale framework.

At each level l , the grid tensor is defined as $\mathcal{A}^{(l)} \in \mathbb{R}^{H^{(l)} \times W^{(l)} \times D^{(l)} \times C^{(l)}}$, where Spatial Dimension ($H^{(l)}, W^{(l)}$) represents spatial resolution (height, width) at level l , Guidance Dimension $D^{(l)}$ specifies the guidance intensity levels at level l and Coefficient Channel $C = 12$ represents a flattened 3×4 affine color transformation matrix.

3.3.2 Guidance Map, Slice Operation, and Multi-Scale Fusion

To achieve adaptive and spatially-varying photometric correction, our multi-scale bilateral grid framework employs a guidance map and a *slicing* operation [4] to retrieve localized transformations, followed by a hierarchical fusion strategy to combine transformations across scales.

We first derive a luminance-based guidance map $I^g(u, v) = \text{GrayScale}(I^r(u, v))$ from the rendered image $I^r(u, v)$, following the approach of [4, 35, 8]. This map encodes spatial brightness variations like shadows and highlights, serving as a spatially-varying query to our multi-scale grid. For each

level l and pixel (u, v) , the luminance d from I^g is used to perform a *slicing* operation, querying the grid’s intensity dimension $D^{(l)}$ to locate an intensity bin. Affine transformation coefficients $\mathcal{A}_{i,j,k}^{(l)}$ around this bin are then combined via trilinear interpolation for a level-specific transformation $\bar{A}^{(l)}(u, v)$. The *slicing* operation retrieves per-pixel transformations from each grid level, written as:

$$\bar{A}^{(l)}(u, v) = \sum_{i,j,k} w_{i,j,k}(u, v, d) \mathcal{A}^s(i, j, k) , \quad (7)$$

To efficiently fuse transformations across scales, we utilize hierarchical function composition. A naive approach of full-resolution *slicing* at each scale is computationally expensive and redundant due to local photometric coherence. To address this, we employ downsampled guidance maps $I^{g(l)}$ for each scale l , performing *slicing* to obtain low-resolution coefficient fields, which are then upsampled. This approach explicitly links scale-aware guidance to patch operations—the reduced-resolution maps enable efficient spatial aggregation of photometric transformations while enhances efficiency (See ablation study in Tab. 5). The level-specific transformations $\mathcal{T}^{(l)}$, decomposed into linear matrices $\bar{M}^{(l)}$ and translations $\bar{T}^{(l)}$, are then sequentially composed from coarse to fine to produce the final composite transformation \bar{A} . The refined image $I^e(u, v)$ is obtained by applying $\bar{A}(u, v)$ to $I^r(u, v)$, with the fusion process expressed as:

$$I^e = \mathcal{T}^{(L-1)} \circ \mathcal{T}^{(L-2)} \circ \dots \circ \mathcal{T}^{(0)}(I^r) , \quad (8)$$

This hierarchical fusion decomposes the photometric transformation into scale-dependent residual refinements. Coarse scales capture global transformations, intermediate scales refine regional variations, and fine scales address local details (Further elaboration in Sec. 4.3). Further details on the interpolation kernel and computational efficiency considerations are provided in Appendix A1.1.

Dataset	Method	Full Image		Human		Vehicle		Geometry		
		PSNR \uparrow	SSIM \uparrow	PSNR \uparrow	SSIM \uparrow	PSNR \uparrow	SSIM \uparrow	CD \downarrow	RMSE \downarrow	Depth \downarrow
Waymo [27]	Baseline	28.92	0.833	25.24	0.681	23.50	0.697	1.482	2.785	0.540
	Baseline w/AC	28.95	0.835	24.92	0.656	23.51	0.699	1.378	2.760	0.519
	Baseline w/BG	28.19	0.831	24.79	0.664	23.09	0.693	1.523	2.798	0.492
	Ours	29.23	0.836	25.55	0.683	23.50	0.707	0.989	2.744	0.477
NuScenes [1]	Baseline	26.37	0.837	26.17	0.774	26.49	0.827	1.458	3.420	0.110
	Baseline w/AC	26.38	0.840	25.83	0.762	26.52	0.828	1.437	3.415	0.106
	Baseline w/BG	25.98	0.837	26.00	0.771	26.10	0.820	1.380	3.390	0.097
	Ours	27.69	0.847	26.53	0.777	27.31	0.834	1.161	3.340	0.059
Argoverse [37]	Baseline	24.59	0.848	23.35	0.743	24.47	0.812	0.954	4.208	0.050
	Baseline w/AC	24.58	0.848	23.22	0.738	24.44	0.811	0.959	4.215	0.051
	Baseline w/BG	23.31	0.842	22.99	0.730	23.49	0.795	0.901	4.218	0.049
	Ours	24.68	0.849	23.35	0.739	24.51	0.827	0.807	4.199	0.040
Pandaset [39]	Baseline	30.20	0.903	29.79	0.830	23.27	0.776	0.503	2.874	0.018
	Baseline w/AC	30.20	0.903	29.64	0.824	23.39	0.783	0.496	2.871	0.020
	Baseline w/BG	29.73	0.904	29.90	0.812	22.22	0.763	0.484	2.867	0.013
	Ours	30.75	0.906	30.18	0.830	23.49	0.784	0.453	2.852	0.011

Table 1: **Comparison with SOTA for scene reconstruction.** w/AC represents appearance codes while w/BG represents single bilateral grids.

4 Experiments

4.1 Experimental Setup

Datasets. We evaluate on four autonomous driving datasets: Waymo [27], NuScenes [1], Argoverse [37], and PandaSet [39], selected for their diversity in sensor configurations (LiDAR, camera specifications), environmental conditions (lighting, seasons), and geographic locations. Identical model hyperparameters are used across all datasets to test generalization capability. Technical specifications including camera counts and ego-vehicle view cropping details are provided in Appendix A2.

Baseline. Our focus is on modeling appearance variance across viewpoints, we build upon the open-source works *DriveStudio* [5], *ChatSim* [36], *StreetGS* [41] and test three approaches: appearance codes, standalone bilateral grids, and our multi-scale bilateral grids. This allows for direct comparison of how each method handles photometric inconsistencies across viewpoints.

Implementation details. We evaluate our method on many autonomous driving datasets to demonstrate its robustness. For each dataset, We train all the methods on a single NVIDIA L40 GPU and

Method	Reconstruction			Novel View Synthesis			Geometry		
	PSNR \uparrow	SSIM \uparrow	LPIPS \downarrow	PSNR \uparrow	SSIM \uparrow	LPIPS \downarrow	CD \downarrow	RMSE \downarrow	Depth \downarrow
ChatSim [36]	25.10	0.805	0.252	23.27	0.725	0.270	1.557	3.509	0.106
ChatSim (Ours)	27.04	0.819	0.231	24.67	0.735	0.249	1.236	3.412	0.053
StreetGS [41]	25.74	0.822	0.240	23.64	0.736	0.259	1.604	3.544	0.107
StreetGS (Ours)	27.90	0.836	0.219	25.10	0.747	0.238	1.272	3.458	0.055

Table 2: **Comparison with different baseline approaches for scene reconstruction.** Performance is reported as the average over the nuScenes [1] scenarios.

compare the 3D reconstruction and novel view synthesis results between camera and LiDAR data. Additionally, we ablate key components of our method and quantify their impact on both appearance and geometry quality.

Training and Dynamic Rendering.

1) Training. To optimize our multi-scale Gaussian scene representation, we employ a joint training strategy that minimizes a composite reconstruction loss :

$$\mathcal{L}_{recon} = \lambda_r \mathcal{L}_1 + \lambda_s \mathcal{L}_{SSIM} + \lambda_d \mathcal{L}_d + \lambda_o \mathcal{L}_o, \quad (9)$$

Furthermore, we introduce two additional regularization terms to enhance image fidelity: *Adaptive Total Variation Regularization*. This term encourages smoothness and reduces noise while preserving image details, and *Circle Regularization Loss*. This loss applies an inverse transformation to the ground-truth images, preventing discrepancies and image quality degradation. As visually demonstrated in Fig. 5, these two terms significantly improve image fidelity. Detailed explanations are provided in Appendix A1.

2) Rendering. For dynamic rendering using our multi-scale bilateral grid framework, we employ a specific interpolation strategy when encountering novel test images, especially those simulating dynamic ISP conditions. Our proposed method first conducts a temporal proximity search to identify the most relevant grids. Following this, we perform scale-specific interpolation using the two nearest grids found. More comprehensive details regarding this interpolation approach are available in Appendix A1.

4.2 Quantitative Evaluation

Reconstruction Quality. We evaluate the reconstruction quality of our method using appearance and geometry metrics, with detailed results presented in Tab. 1.

(1) Appearance Fidelity. Our approach demonstrates superior performance in appearance-based metrics (PSNR and SSIM). As shown in Tab. 1, our method achieves the highest PSNR and SSIM scores for full image reconstruction across all tested datasets (Waymo, NuScenes, Argoverse, and Pandaset). Furthermore, when evaluating segmented dynamic regions such as humans and vehicles, our method largely surpasses the baselines, indicating its robustness in capturing both global scene appearance and fine-grained details of dynamic objects. For instance, on NuScenes, our PSNR for 'Vehicle' is 27.31, compared to the best baseline score of 26.52. While there are isolated cases where a baseline performs comparably or slightly better (e.g., Human SSIM on Argoverse), our method generally offers the most consistent and highest quality appearance reconstruction.

(2) Geometric Accuracy. In terms of geometric fidelity, our method consistently outperforms all baselines across all datasets, as evidenced by the Chamfer Distance (CD), Root Mean Square Error (RMSE), and Depth L2 Error metrics in Tab. 1. For example, on the Waymo dataset, our method achieves a CD of 0.989, significantly lower than the best baseline score of 1.378. This superior geometric accuracy is partly attributed to our model's improved handling of "floater" artifacts, leading to more precise LiDAR representations, as qualitatively illustrated in Fig. 4.

Dataset	Method	PSNR \uparrow		
		Full Image	Human	Vehicle
Waymo [27]	Baseline	26.40	23.91	21.25
	Baseline w/AC	26.44	23.81	21.34
	Baseline w/BG	21.51	22.91	19.82
	Ours	26.55	23.97	21.36
NuScenes [1]	Baseline	23.74	23.55	22.80
	Baseline w/AC	23.74	23.35	22.84
	Baseline w/BG	23.60	23.63	22.79
	Ours	24.64	23.75	23.22
Argoverse [37]	Baseline	22.53	20.73	20.84
	Baseline w/AC	22.51	20.70	20.80
	Baseline w/BG	21.70	20.67	20.59
	Ours	22.58	20.79	20.86
Pandaset [39]	Baseline	27.49	26.94	21.02
	Baseline w/AC	27.51	26.98	21.13
	Baseline w/BG	27.38	27.08	20.77
	Ours	27.89	27.22	21.32

Table 3: **Comparison on Novel View Synthesis.**

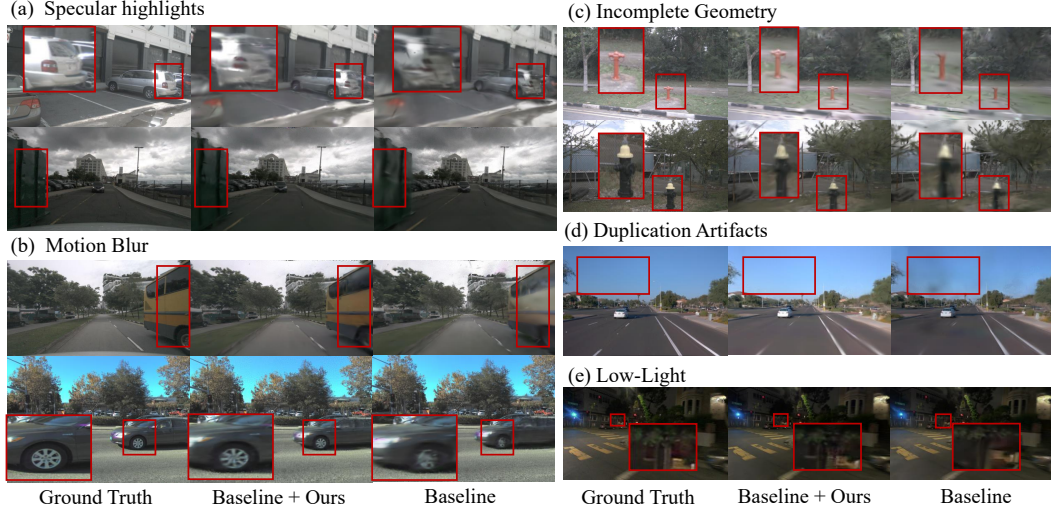


Figure 3: Visualizations of our method and baseline methods on Waymo [27], NuScenes [1], Argoverse [37], and PandaSet [39] dataset.

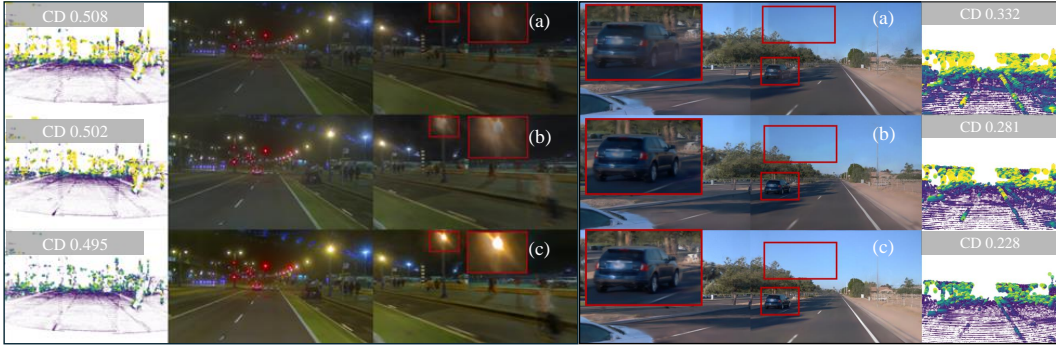


Figure 4: Our proposed framework (c) outperforms appearance codes (a) and single bilateral grids (b) by simultaneously addressing optimization challenges and enhancing geometric modeling. This delivers significant geometric accuracy improvements (lower Chamfer Distance (CD) via multi-scale bilateral grid, reducing error and improving reconstruction) and reduced photometric inconsistency (fewer floaters) in dynamic, decoupled driving scenes. **Yellow** indicates a high lidar error, while **Purple** indicates a low lidar error.

Novel View Synthesis. The performance of our method in novel view synthesis is detailed in Tab. 3. Our approach consistently achieves the highest PSNR scores across all datasets for full images as well as for segmented human and vehicle categories. For example, on the NuScenes dataset, our method achieves a PSNR of 24.64 for the full image, 23.75 for humans, and 23.22 for vehicles, outperforming all baseline variations. This underscores the capability of our method to generate high-fidelity novel views from new camera poses.

Comparison with State-of-the-Art Methods. To further assess the benefits of our architectural contributions, we integrated our core components into two recent state-of-the-art methods: ChatSim [36] and StreetGS [41]. The comparative results, averaged over NuScenes scenarios, are presented in Tab. 2.

When our enhancements are applied (denoted as "ChatSim (Ours)" and "StreetGS (Ours)"), both methods exhibit significant improvements across all evaluated aspects. For instance, integrating our approach with ChatSim improves its reconstruction PSNR from 25.10 to 27.04 and its novel view synthesis PSNR from 23.27 to 24.67. Similarly, StreetGS sees its reconstruction PSNR boosted from 25.74 to 27.90 and its Chamfer Distance reduced from 1.604 to 1.272. These results highlight

the generalizability and effectiveness of our proposed techniques, demonstrating their capability to enhance the performance of existing strong baseline models for comprehensive scene understanding and representation.

4.3 Qualitative Evaluation

Rendering Results. Fig. 3 presents visualization results of our method on scenes from Waymo [27], NuScenes [1], Argoverse [37], and PandaSet [39], demonstrating its capability to handle diverse conditions that might otherwise lead to inconsistencies.

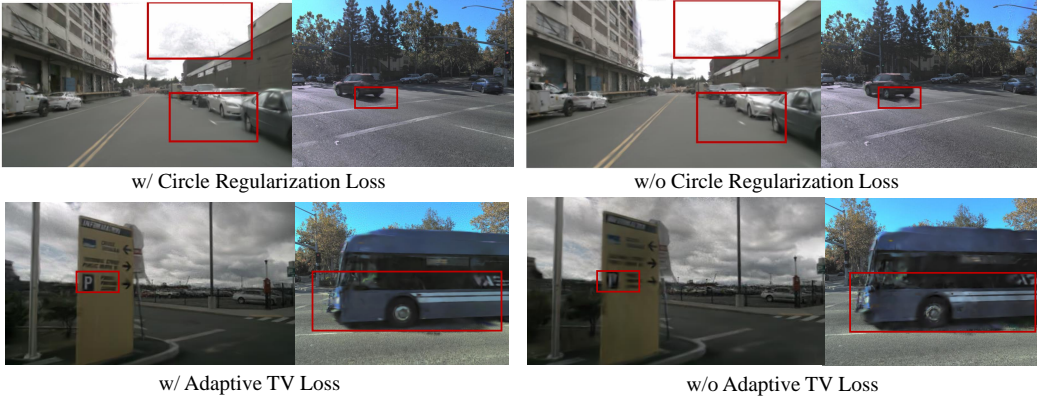


Figure 5: Visualizations of ablations on Circle Regularization loss and Adaptive TV loss.

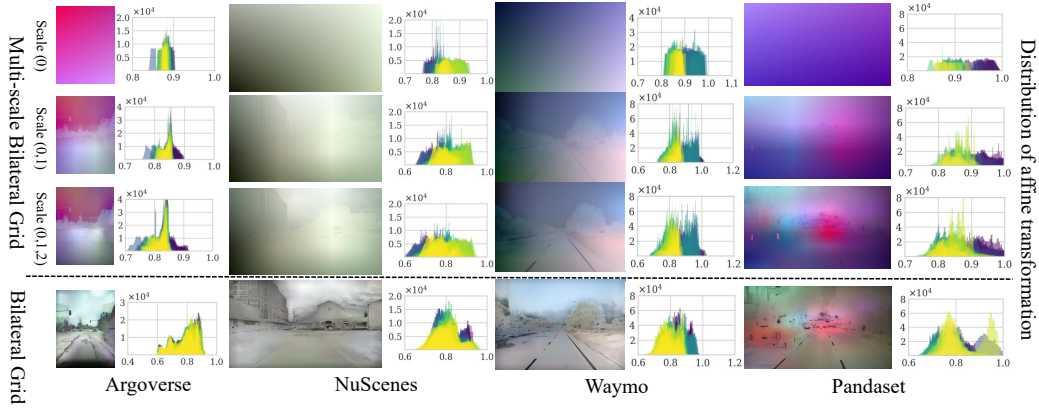


Figure 6: **Visualization of Affine Transformations and Distributions.** The first three rows display the affine transformation results and corresponding distributions when applying the first level (scale 0), the first two levels (scales 0-1), and all three levels (scales 0-1-2) of our multi-scale approach. The final row compares these to results from a single bilateral grid, demonstrating that the multi-scale bilateral grid achieves a coarse-to-fine, smooth image enhancement with more diverse processing capabilities.

Affine Transformations Distributions. According to Fig. 6, analyzing grayscale histograms of learned affine transformations reveals a key distinction between original single-scale and our multi-scale bilateral grids. For the original grid, each viewpoint’s histogram typically exhibits two distinct peaks. This bi-modal distribution suggests a focused, somewhat limited photometric adaptation. It implies that for each view, correction focuses on a few dominant transformations. More visualization results are shown at Fig. 3. A particularly interesting observation arises examining histograms of our multi-scale grid’s coarsest level. Intriguingly, these histograms also demonstrate peaky distributions, varying significantly across viewpoints. This isn’t contradictory, but insightful: even at its coarsest level, the grid learns view-dependent base appearances. The coarse grid captures

dominant, scene-wide photometric transformations characteristic of each viewpoint. Peaks in coarse-level histograms likely represent these primary, global photometric adjustments, tailored per view.

However, the key advantage is evident in the overlaid histogram, which aggregates distributions from all multi-scale levels and viewpoints. This histogram is notably flatter and more dispersed than those of the original grid, a characteristic directly resulting from hierarchical and residual refinement. Our framework first uses the coarse grid to establish a view-dependent base appearance. Subsequently, medium and fine grids learn residual transformations to correct coarse grid errors. Medium grids then refine regional photometric variations, while fine grids handle local, pixel-level details. This layered, residual approach significantly broadens the spectrum of learnable photometric transformations. The original grid’s two-peaked histograms signify its narrow adaptation. In contrast, the multi-scale version’s flatter histogram reveals its core strength: a diverse, generalizable, and robust representation of spatially-varying photometric transformations. This enhanced representation is crucial for consistent and high-quality renderings across diverse driving views.

4.4 Ablation Studies

As shown in Tab. 4, Tab. 5 and Fig. 5, we systematically evaluate component contributions through:

Guidance Map Resolution. Varying guidance map resolution shows a trade-off in performance. Using the highest resolution (1,1,1) results in a slightly lower NVS PSNR compared to using (2,2,1) which achieves the highest NVS PSNR(24.64) in these ablations, demonstrating our patch-based approach balances efficiency and effectiveness. **Grid Size Combinations.** Using different combinations of grid sizes significantly impacts geometry, as indicated by CD. Combining smaller grids like (2,2,1)+(4,4,2) results in a lower CD (1.213) than using combinations including larger grids or the combination with the largest grid (4,4,2)+(8,8,4)+(16,16,8). **Loss Functions.** Ablating the circle regularization loss slightly reduces both Reconstruction PSNR (from 27.69 to 27.47) and NVS PSNR (from 24.64 to 24.52). Removing the adaptive total variance loss has a minimal impact on rendering result. **Efficiency.** As shown in Tab. 4, while the ‘Baseline w/BG’ dramatically increases parameters and training time, our method achieves a much more moderate increase in parameters and training time (to 2.10 hours) relative to the lightweight appearance codes. With multi-scale bilateral grid guided training, we found the rendering speed may improve due to the decreased number of unnecessary Gaussians.

5 Conclusion

We propose a multi-scale bilateral grid seamlessly integrating global appearance codes and pixel-wise bilateral grids to address photometric inconsistencies in autonomous driving neural rendering.

Limitations. While our proposed multi-scale bilateral grid demonstrates significant improvements in handling photometric inconsistencies and enhancing geometric accuracy in driving scene reconstruction, certain limitations warrant discussion. (1) The computational remains higher than simpler appearance code techniques; this could be a factor in highly resource-constrained deployment scenarios. (2) while effective for many dynamic elements, modeling extremely complex, fast-moving, or highly non-rigid objects with complete fidelity remains an ongoing challenge.

Configuration	Grid Params (M)	Training Time (h)	Testing time (FPS)
Baseline w/AC	0.072	1.93	53
Baseline w/BG	27.843	2.85	54 / 38†
Ours	3.969	2.10	54 / 42†

Table 4: **Computational Efficiency Analysis.**

† means using bilateral grids processing during rendering.

Settings	Recon.↑	NVS.↑	CD ↓
Full model	27.69	24.64	1.161
<i>(a) Guidance Map Resolution</i>			
(1,1,1)	27.62	24.34	1.271
(2,2,1)	27.68	24.64	1.170
(8,8,4)	27.52	24.53	1.187
(16,16,8)	27.50	24.54	1.202
<i>(b) Grid Size Combinations</i>			
(4,4,2)+(8,8,4)	27.49	24.56	1.963
(2,2,1)+(8,8,4)	27.57	24.57	1.940
(2,2,1)+(4,4,2)	27.33	24.42	1.213
(4,4,2)+(8,8,4)+(16,16,8)	27.31	24.46	2.297
<i>(c) Loss Functions</i>			
w/o circle regularization loss	27.47	24.52	1.164
w/o adaptive total variance loss	27.64	24.61	1.169

Table 5: **Ablations.** Numbers in *Guidance Map Resolution* settings indicate downsample factors from coarse level to fine level, and numbers in *Grid Size Combinations* settings indicate grid size.

References

- [1] Holger Caesar, Varun Bankiti, Alex H Lang, Sourabh Vora, Venice Erin Liong, Qiang Xu, Anush Krishnan, Yu Pan, Giancarlo Baldan, and Oscar Beijbom. nuscenes: A multimodal dataset for autonomous driving. In *Proceedings of the IEEE/CVF conference on computer vision and pattern recognition*, pages 11621–11631, 2020.
- [2] Danpeng Chen, Hai Li, Weicai Ye, Yifan Wang, Weijian Xie, Shangjin Zhai, Nan Wang, Haomin Liu, Hujun Bao, and Guofeng Zhang. Pgsr: Planar-based gaussian splatting for efficient and high-fidelity surface reconstruction. *IEEE Transactions on Visualization and Computer Graphics*, 2024.
- [3] Jiawen Chen, Andrew Adams, Neal Wadhwa, and Samuel W Hasinoff. Bilateral guided upsampling. *ACM Transactions on Graphics (TOG)*, 35(6):1–8, 2016.
- [4] Jiawen Chen, Sylvain Paris, and Frédo Durand. Real-time edge-aware image processing with the bilateral grid. *ACM Transactions on Graphics (TOG)*, 26(3):103–es, 2007.
- [5] Ziyu Chen, Jiawei Yang, Jiahui Huang, Riccardo de Lutio, Janick Martinez Esturo, Boris Ivanovic, Or Litany, Zan Gojcic, Sanja Fidler, Marco Pavone, et al. Omnire: Omni urban scene reconstruction. *arXiv preprint arXiv:2408.16760*, 2024.
- [6] Kai Cheng, Xiaoxiao Long, Kaizhi Yang, Yao Yao, Wei Yin, Yuexin Ma, Wenping Wang, and Xuejin Chen. Gaussianpro: 3d gaussian splatting with progressive propagation. In *Forty-first International Conference on Machine Learning*, 2024.
- [7] Frédo Durand and Julie Dorsey. Fast bilateral filtering for the display of high-dynamic-range images. In *Proceedings of the 29th annual conference on Computer graphics and interactive techniques*, pages 257–266, 2002.
- [8] Michaël Gharbi, Jiawen Chen, Jonathan T Barron, Samuel W Hasinoff, and Frédo Durand. Deep bilateral learning for real-time image enhancement. *ACM Transactions on Graphics (TOG)*, 36(4):1–12, 2017.
- [9] Georg Hess, Carl Lindström, Maryam Fatemi, Christoffer Petersson, and Lennart Svensson. Splatad: Real-time lidar and camera rendering with 3d gaussian splatting for autonomous driving. *arXiv preprint arXiv:2411.16816*, 2024.
- [10] Wonbong Jang and Lourdes Agapito. Codenerf: Disentangled neural radiance fields for object categories. In *Proceedings of the IEEE/CVF International Conference on Computer Vision*, pages 12949–12958, 2021.
- [11] Bu Jin, Yupeng Zheng, Pengfei Li, Weize Li, Yuhang Zheng, Sujie Hu, Xinyu Liu, Jinwei Zhu, Zhijie Yan, Haiyang Sun, et al. Tod3cap: Towards 3d dense captioning in outdoor scenes. In *European Conference on Computer Vision*, pages 367–384. Springer, 2024.
- [12] Bernhard Kerbl, Georgios Kopanas, Thomas Leimkühler, and George Drettakis. 3d gaussian splatting for real-time radiance field rendering. *ACM Trans. Graph.*, 42(4):139–1, 2023.
- [13] Jonas Kulhanek, Songyou Peng, Zuzana Kukelova, Marc Pollefeys, and Torsten Sattler. Wildgaussians: 3d gaussian splatting in the wild. *arXiv preprint arXiv:2407.08447*, 2024.
- [14] Bohan Li, Jiajun Deng, Wenyao Zhang, Zhujin Liang, Dalong Du, Xin Jin, and Wenjun Zeng. Hierarchical temporal context learning for camera-based semantic scene completion. In *European Conference on Computer Vision*, pages 131–148. Springer, 2024.
- [15] Bohan Li, Jiazhe Guo, Hongsi Liu, Yingshuang Zou, Yikang Ding, Xiwu Chen, Hu Zhu, Feiyang Tan, Chi Zhang, Tiancai Wang, et al. Uniscene: Unified occupancy-centric driving scene generation. *arXiv preprint arXiv:2412.05435*, 2024.
- [16] Zhuopeng Li, Yilin Zhang, Chenming Wu, Jianke Zhu, and Liangjun Zhang. Ho-gaussian: Hybrid optimization of 3d gaussian splatting for urban scenes. In *European Conference on Computer Vision*, pages 19–36. Springer, 2024.
- [17] Carl Lindström, Georg Hess, Adam Lilja, Maryam Fatemi, Lars Hammarstrand, Christoffer Petersson, and Lennart Svensson. Are nerfs ready for autonomous driving? towards closing the real-to-simulation gap. In *Proceedings of the IEEE/CVF Conference on Computer Vision and Pattern Recognition*, pages 4461–4471, 2024.
- [18] Junchen Liu, Wenbo Hu, Zhuo Yang, Jianteng Chen, Guoliang Wang, Xiaoxue Chen, Yantong Cai, Huan-gao Gao, and Hao Zhao. Rip-nerf: Anti-aliasing radiance fields with ripmap-encoded platonic solids. In *ACM SIGGRAPH 2024 Conference Papers*, pages 1–11, 2024.

- [19] Yifan Lu, Xuanchi Ren, Jiawei Yang, Tianchang Shen, Zhangjie Wu, Jun Gao, Yue Wang, Siheng Chen, Mike Chen, Sanja Fidler, et al. Infinitcube: Unbounded and controllable dynamic 3d driving scene generation with world-guided video models. *arXiv preprint arXiv:2412.03934*, 2024.
- [20] Nicolas Märki, Federico Perazzi, Oliver Wang, and Alexander Sorkine-Hornung. Bilateral space video segmentation. In *Proceedings of the IEEE conference on computer vision and pattern recognition*, pages 743–751, 2016.
- [21] Ricardo Martin-Brualla, Noha Radwan, Mehdi SM Sajjadi, Jonathan T Barron, Alexey Dosovitskiy, and Daniel Duckworth. Nerf in the wild: Neural radiance fields for unconstrained photo collections. In *Proceedings of the IEEE/CVF conference on computer vision and pattern recognition*, pages 7210–7219, 2021.
- [22] Ben Mildenhall, Pratul P Srinivasan, Matthew Tancik, Jonathan T Barron, Ravi Ramamoorthi, and Ren Ng. Nerf: Representing scenes as neural radiance fields for view synthesis. *Communications of the ACM*, 65(1):99–106, 2021.
- [23] Thang-Anh-Quan Nguyen, Luis Roldão, Nathan Piasco, Moussab Bennehar, and Dzmitry Tsishkou. Rodus: Robust decomposition of static and dynamic elements in urban scenes. In *European Conference on Computer Vision*, pages 112–130. Springer, 2024.
- [24] James Okae, Bohan Li, Juan Du, and Yueming Hu. Robust scale-aware stereo matching network. *IEEE Transactions on Artificial Intelligence*, 3(2):244–253, 2021.
- [25] Sylvain Paris and Frédo Durand. A fast approximation of the bilateral filter using a signal processing approach. In *Computer Vision–ECCV 2006: 9th European Conference on Computer Vision, Graz, Austria, May 7–13, 2006, Proceedings, Part IV 9*, pages 568–580. Springer, 2006.
- [26] Xiaowei Song, Jv Zheng, Shiran Yuan, Huan-ang Gao, Jingwei Zhao, Xiang He, Weihao Gu, and Hao Zhao. Sa-gs: Scale-adaptive gaussian splatting for training-free anti-aliasing. *arXiv preprint arXiv:2403.19615*, 2024.
- [27] Pei Sun, Henrik Kretzschmar, Xerxes Dotiwalla, Aurelien Chouard, Vijaysai Patnaik, Paul Tsui, James Guo, Yin Zhou, Yuning Chai, Benjamin Caine, et al. Scalability in perception for autonomous driving: Waymo open dataset. In *Proceedings of the IEEE/CVF conference on computer vision and pattern recognition*, pages 2446–2454, 2020.
- [28] Matthew Tancik, Vincent Casser, Xinchun Yan, Sabeek Pradhan, Ben Mildenhall, Pratul P Srinivasan, Jonathan T Barron, and Henrik Kretzschmar. Block-nerf: Scalable large scene neural view synthesis. In *Proceedings of the IEEE/CVF Conference on Computer Vision and Pattern Recognition*, pages 8248–8258, 2022.
- [29] Tang Tao, Longfei Gao, Guangrun Wang, Yixing Lao, Peng Chen, Hengshuang Zhao, Dayang Hao, Xiaodan Liang, Mathieu Salzmann, and Kaicheng Yu. Lidar-nerf: Novel lidar view synthesis via neural radiance fields. In *Proceedings of the 32nd ACM International Conference on Multimedia*, pages 390–398, 2024.
- [30] Tang Tao, Guangrun Wang, Yixing Lao, Peng Chen, Jie Liu, Liang Lin, Kaicheng Yu, and Xiaodan Liang. Alignmif: Geometry-aligned multimodal implicit field for lidar-camera joint synthesis. In *Proceedings of the IEEE/CVF Conference on Computer Vision and Pattern Recognition*, pages 21230–21240, 2024.
- [31] Beiwen Tian, Mingdao Liu, Huan-ang Gao, Pengfei Li, Hao Zhao, and Guyue Zhou. Unsupervised road anomaly detection with language anchors. In *2023 IEEE international conference on robotics and automation (ICRA)*, pages 7778–7785. IEEE, 2023.
- [32] Adam Tonderski, Carl Lindström, Georg Hess, William Ljungbergh, Lennart Svensson, and Christoffer Petersson. Neurad: Neural rendering for autonomous driving. In *Proceedings of the IEEE/CVF Conference on Computer Vision and Pattern Recognition*, pages 14895–14904, 2024.
- [33] Nan Wang, Xiaohan Yan, Xiaowei Song, and Zhicheng Wang. Semantic-guided gaussian splatting with deferred rendering. In *ICASSP 2025-2025 IEEE International Conference on Acoustics, Speech and Signal Processing (ICASSP)*, pages 1–5. IEEE, 2025.
- [34] Peng Wang, Lingjie Liu, Yuan Liu, Christian Theobalt, Taku Komura, and Wenping Wang. Neus: Learning neural implicit surfaces by volume rendering for multi-view reconstruction. *arXiv preprint arXiv:2106.10689*, 2021.
- [35] Yuehao Wang, Chaoyi Wang, Bingchen Gong, and Tianfan Xue. Bilateral guided radiance field processing. *ACM Transactions on Graphics (TOG)*, 43(4):1–13, 2024.

- [36] Yuxi Wei, Zi Wang, Yifan Lu, Chenxin Xu, Changxing Liu, Hao Zhao, Siheng Chen, and Yanfeng Wang. Editable scene simulation for autonomous driving via collaborative llm-agents. In *Proceedings of the IEEE/CVF Conference on Computer Vision and Pattern Recognition*, pages 15077–15087, 2024.
- [37] Benjamin Wilson, William Qi, Tanmay Agarwal, John Lambert, Jagjeet Singh, Siddhesh Khandelwal, Bowen Pan, Ratnesh Kumar, Andrew Hartnett, Jhony Kaesemodel Pontes, et al. Argoverse 2: Next generation datasets for self-driving perception and forecasting. *arXiv preprint arXiv:2301.00493*, 2023.
- [38] Zirui Wu, Tianyu Liu, Liyi Luo, Zhide Zhong, Jianteng Chen, Hongmin Xiao, Chao Hou, Haozhe Lou, Yuantao Chen, Runyi Yang, et al. Mars: An instance-aware, modular and realistic simulator for autonomous driving. In *CAAI International Conference on Artificial Intelligence*, pages 3–15. Springer, 2023.
- [39] Pengchuan Xiao, Zhenlei Shao, Steven Hao, Zishuo Zhang, Xiaolin Chai, Judy Jiao, Zesong Li, Jian Wu, Kai Sun, Kun Jiang, et al. Pandaset: Advanced sensor suite dataset for autonomous driving. In *2021 IEEE international intelligent transportation systems conference (ITSC)*, pages 3095–3101. IEEE, 2021.
- [40] Bin Xu, Yuhua Xu, Xiaoli Yang, Wei Jia, and Yulan Guo. Bilateral grid learning for stereo matching networks. In *Proceedings of the IEEE/CVF Conference on Computer Vision and Pattern Recognition*, pages 12497–12506, 2021.
- [41] Yunzhi Yan, Haotong Lin, Chenxu Zhou, Weijie Wang, Haiyang Sun, Kun Zhan, Xianpeng Lang, Xiaowei Zhou, and Sida Peng. Street gaussians: Modeling dynamic urban scenes with gaussian splatting. In *European Conference on Computer Vision*, pages 156–173. Springer, 2024.
- [42] Ziyang Yan, Wenzhen Dong, Yihua Shao, Yuhang Lu, Liu Haiyang, Jingwen Liu, Haozhe Wang, Zhe Wang, Yan Wang, Fabio Remondino, et al. Renderworld: World model with self-supervised 3d label. *arXiv preprint arXiv:2409.11356*, 2024.
- [43] Yifan Yang, Shuhai Zhang, Zixiong Huang, Yubing Zhang, and Minghui Tan. Cross-ray neural radiance fields for novel-view synthesis from unconstrained image collections. In *Proceedings of the IEEE/CVF International Conference on Computer Vision*, pages 15901–15911, 2023.
- [44] Zehao Yu, Songyou Peng, Michael Niemeyer, Torsten Sattler, and Andreas Geiger. Monosdf: Exploring monocular geometric cues for neural implicit surface reconstruction. *Advances in neural information processing systems*, 35:25018–25032, 2022.
- [45] Shiran Yuan and Hao Zhao. Slimmerf: Slimmable radiance fields. In *2024 International Conference on 3D Vision (3DV)*, pages 64–74. IEEE, 2024.
- [46] Dongbin Zhang, Chuming Wang, Weitao Wang, Peihao Li, Minghan Qin, and Haoqian Wang. Gaussian in the wild: 3d gaussian splatting for unconstrained image collections. In *European Conference on Computer Vision*, pages 341–359. Springer, 2024.
- [47] Saining Zhang, Baijun Ye, Xiaoxue Chen, Yuantao Chen, Zongzheng Zhang, Cheng Peng, Yongliang Shi, and Hao Zhao. Drone-assisted road gaussian splatting with cross-view uncertainty. *arXiv preprint arXiv:2408.15242*, 2024.
- [48] Zhuoran Zheng, Wenqi Ren, Xiaochun Cao, Xiaobin Hu, Tao Wang, Fenglong Song, and Xiuyi Jia. Ultra-high-definition image dehazing via multi-guided bilateral learning. In *2021 IEEE/CVF Conference on Computer Vision and Pattern Recognition (CVPR)*, pages 16180–16189. IEEE, 2021.
- [49] Hongyu Zhou, Jiahao Shao, Lu Xu, Dongfeng Bai, Weichao Qiu, Bingbing Liu, Yue Wang, Andreas Geiger, and Yiyi Liao. Hugs: Holistic urban 3d scene understanding via gaussian splatting. In *Proceedings of the IEEE/CVF Conference on Computer Vision and Pattern Recognition*, pages 21336–21345, 2024.
- [50] Xiaoyu Zhou, Zhiwei Lin, Xiaojun Shan, Yongtao Wang, Deqing Sun, and Ming-Hsuan Yang. Drivinggaussian: Composite gaussian splatting for surrounding dynamic autonomous driving scenes. In *Proceedings of the IEEE/CVF Conference on Computer Vision and Pattern Recognition*, pages 21634–21643, 2024.